Probing the circulation of ring-shaped Bose-Einstein condensates

Noel Murray,[1] Michael Krygier,[1] Mark Edwards,[1] K. C. Wright,[2] G. K. Campbell,[2] and Charles W. Clark[2]

[1]*Department of Physics, Georgia Southern University, Statesboro, Georgia 30460-8031, USA*

[2]*Joint Quantum Institute, National Institute of Standards and Technology and the University of Maryland,*
Gaithersburg, Maryland 20899, USA

This paper reports the results of a theoretical and experimental study of how the initial circulation of ring-shaped Bose-Einstein condensates (BECs) can be probed by time-of-flight (TOF) images. We have studied the dynamics of a BEC after release from a toroidal trap potential by solving the three-dimensional Gross-Pitaevskii (GP) equation. The trap and condensate characteristics matched those of a recent experiment. The circulation, experimentally imparted to the condensate by stirring, was simulated by imprinting a linear azimuthal phase on the initial condensate wave function. The simulated TOF images were in good agreement with the experimental data. We find that upon release the dynamics of the ring-shaped condensate proceeds in two distinct phases. First, the condensate expands rapidly inward, filling in the initial hole until it reaches a minimum radius that depends on the initial circulation. In the second phase, the density at the inner radius increases to a maximum after which the hole radius begins slowly to expand. During this second phase a series of concentric rings appears due to the interference of ingoing and outgoing matter waves from the inner radius. The results of the GP equation predict that the hole area is a quadratic function of the initial circulation when the condensate is released directly from the trap in which it was stirred and is a linear function of the circulation if the trap is relaxed before release. These scalings matched the data. Thus hole size after TOF can be used as a reliable probe of initial condensate circulation. This connection between circulation and hole size after TOF will facilitate future studies of atomtronic systems that are implemented in ultracold quantum gases.

I. INTRODUCTION

Recently, there has been much research activity devoted to "atomtronic" systems: confined ultracold atomic gases that are analogous to electronic devices and circuits [1,2]. Atomtronic devices rely on neutral atoms, often Bose Einstein condensed, for their operation. Characteristics of the atoms in these devices include tunable collisional interactions, internal structure, long-range coherence, and superfluidity. Thus atom-gas analogs of quite a number of electronic devices have been proposed including diodes [3,4] and transistors [5], and a capacitor discharged through a resistor [6,7]. The coherence and superfluid properties of these systems make them useful as sensors and other devices that can take advantage of superfluidity.

Of particular interest is the realization of an atomic-gas analog of a superconducting quantum interference device (SQUID). Traditional SQUIDs are used to construct magnetic-field detectors, voltmeters, gradiometers, and a host of other metrologic devices [8]. SQUID circuits have been realized with either tunnel or weak-link junctions [9,10]. In gaseous Bose-Einstein condensates (BECs), Josephson-like junctions have been demonstrated in double-well potentials [11,12] and a closed-loop atom "circuit" was implemented in a ring-shaped confining potential [13].

Recently, an atom circuit analogous to an rf SQUID [8] was implemented in a ring BEC by creating a rotating weak link (a region of reduced superfluid density) with a blue-detuned laser beam [14]. In that experiment, the rotating weak link was used to drive phase slips which changed the circulation around the ring. In order to measure the circulation, the condensate was released from the trap allowing it to expand in time of flight (TOF). The image of the resulting condensate exhibited

a smooth density profile for zero circulation and a hole whose size depended on the winding number m (the number of times the phase winds through 2π in a closed loop around the ring) for nonzero circulation. The winding numbers of released condensates were inferred by measuring the distribution of hole areas in the TOF images.

In this paper we present an experimental and theoretical study of the connection between the condensate winding number at the time of release with the size of the hole in the TOF image. This connection has important consequences for the field of atomtronics since it provides a solid theoretical foundation for the formulation of models that can underly the analogies between electric circuits and ultracold atomic-gas systems, as seen, for example, in Ref. [14].

The plan of the paper is as follows. In Sec. II we describe the conditions of the experiment where ring-shaped condensates were created, stirred, released, and imaged. Typical results from these experiments are also displayed. Section III describes the modeling of the experiment based on the Gross-Pitaevskii (GP) equation and Sec. IV shows a comparison of experiment with GP simulations. We found that simulations based on the GP equation matched the data well. Having established that the GP equation can provide a good description of condensate behavior under these conditions, we present the GP-equation picture of the dynamics of a released ring BEC as a function of its initial winding number. Finally, Sec. VI provides a summary of the results and places the result in context.

II. DESCRIPTION OF THE EXPERIMENT

The ring BEC, shown in Fig. 1(a), contains $\approx 4 \times 10^5$ ^{23}Na atoms, spin polarized in the $3^2 S_{1/2} |F = 1, m_F = -1\rangle$ state.
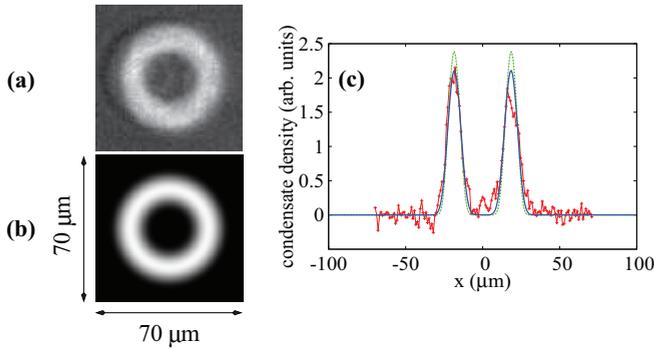
FIG. 1. (Color online) (a) *In situ* 2D density image of the initial condensate used to determine the parameters of the confining potential. (b) The 2D density image of the TIGPE theoretical result, and (c) cut-through density profiles comparing the experimental data (red curve with points explicitly displayed), the fitted solution of the TIGPE (green, dotted curve), and the fitted solution (blue, solid curve) blurred by convolving it with a Gaussian having a 4 μm $1/e^2$ radius.

The atoms are held in an optical dipole trapping potential formed by a combination of up to three laser beams. Two of these trapping beams are red detuned from atomic resonance: a horizontal "sheet" beam providing the primary confinement in the vertical direction with trap frequency $\omega_z/2\pi = 600$ Hz, and a vertically propagating LG_0^1 "ring" beam, which can be used to create a toroidal potential minimum. This red-detuned trap configuration was used previously for experiments conducted in the same laboratory [13,14]. An alternative setup, which uses a vertically propagating blue-detuned "antiring" beam formed by reimaging the light transmitted through a ring-shaped intensity mask onto the BEC, is now used to provide a ring-shaped trap during experiments. This blue-detuned trap allows the BEC to be confined to a narrower annulus than the red trap with a smoother trap minimum.

As described below, the blue-detuned trap is now used for performing experiments, and the red-detuned LG_0^1 beam is added only to facilitate loading and releasing the blue-detuned ring trap. If the imaging resolution were perfect, the blue-detuned trap would be hard walled; however, the 4 μm resolution of the imaging system blurs the edges of the trap. With our narrow annulus, the shadow in the intensity pattern can be approximated by a two-dimensional (2D) Gaussian ring with a $1/e^2$ radius of 9(1) μm and mean radius of 18.5(1) μm. This smooth, narrow annular trap can support stable persistent currents of up to winding number $m = 12$ (see below).

For this experiment, the atomic sample was initially trapped and cooled to below the BEC transition in the red-detuned ring trap, primarily by ramping down the intensity of the sheet beam. After the BEC was formed, the blue-detuned ring was ramped up to its full value while keeping the red-detuned ring on after which the red-detuned ring was ramped off. The BEC was then driven into a circulating state by stirring it with a tightly focused blue-detuned beam propagating in the vertical direction. The position and intensity of this beam was controlled by an acousto-optic deflector, using the same time-averaged scanning technique reported in Ref. [14], which creates a broad, effectively flat potential in the radial direction.

The height of the (initially stationary) potential barrier was ramped up over 200 ms to a height above the chemical potential of the BEC. Once at full height, the barrier was accelerated in the azimuthal direction around the ring up to a final angular velocity Ω, which could be varied between 0 and 15 Hz. After this period of acceleration, the velocity was held constant while the barrier height was ramped to zero over 200 ms, allowing the condensate to reconnect around the ring.

Immediately following this stirring procedure, the condensate was often in a highly excited state with one or more vortex excitations in the annulus. We therefore allowed 5.65 s of hold time for those excitations to damp out [15], leaving the BEC in a simple, vortex-free persistent current state.

Once the BEC was prepared in a circulating state, one of two procedures was followed to allow the condensate to expand prior to absorption imaging. In the first case, the trapping beams were turned off suddenly (<1 μs), and the condensate was allowed to expand for 10 ms TOF. In the second case, the red-detuned ring trap was turned back on, and then the radial confinement of the condensate was relaxed to allow atoms to fill in the center of the ring prior to the 10 ms TOF.

This more complex release scheme was developed to make the central hole associated with the persistent current visible earlier in TOF expansion. In experiments using the blue-detuned trap the handoff back to the red trap is required because lowering of the blue-detuned ring confinement alone allows atoms to escape the central trap region into the periphery of the sheet trap. To execute this handoff in this experiment, we first turned the red-detuned ring trap back on over 200 ms, and then ramped the blue-detuned ring off in 300 ms, and finally ramped the red-detuned ring down to about 10% of its typical power in 50 ms. Imaging of the BEC was done using partial-transfer absorption imaging [13].

A representative set of experimental TOF images is shown in Fig. 3 for the direct-release procedure, and in Fig. 4 for the radial relaxation procedure. The phase winding number of the persistent current for each run of the experiment was determined by measuring the hole sizes for all runs for a given release procedure (i.e., either direct release or radial relaxation) and making a histogram plot of these to obtain the distribution of hole sizes.

There were approximately 100 experimental runs for each release procedure, as shown in Fig. 2. The histograms displayed in that figure show that the hole sizes cluster around discrete values and that the spaces between these clusters exhibit clear gaps. This hole-size behavior enables the assignment of a winding number, m, to each cluster starting with $m = 0$ for the cluster centered at the smallest area and increasing sequentially. The measured hole area was also affected by the imaging resolution, particularly for the direct-release images shown in Fig. 3 and for small values of m where the 4 μm resolution is comparable to the size of the hole. The stirring speed was varied in such a way as to ensure that many samples were obtained for each winding number in the expected range.

III. SIMULATING THE EXPERIMENT

To simulate the experiment we divided it into three distinct phases. These were (1) forming the initial condensate, (2) stirring the condensate to give it a nonzero circulation, and (3) probing the condensate by releasing it and allowing it to
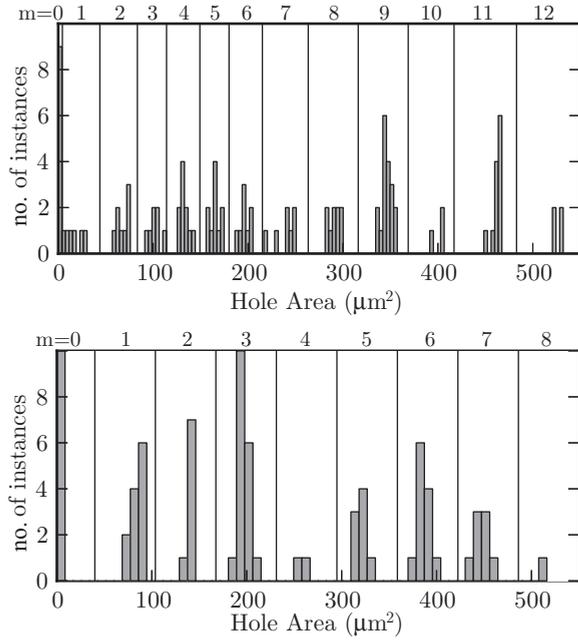
FIG. 2. Circulation of stirred condensates was determined experimentally from the distribution of hole sizes in the expanded cloud. These distributions are shown in the histograms above for the direct-release case (upper) and for the ramp-and-release cases (lower). The winding number m assigned for a given hole area is labeled for each bin.

expand before imaging. To simulate phase one we determined the initial condensate wave function by solving the time-independent, Gross-Pitaevskii equation (TIGPE). The values of the parameters of the model potential used in the TIGPE were determined by varying them until the density profile of the solution matched the experimental profile of the *in situ* condensate, as shown in Fig. 1.

In phase two the result of stirring the condensate was simulated by multiplying its wave function by $e^{im\phi}$, where ϕ is the azimuthal angle in cylindrical coordinates. This adds m units of circulation to the condensate (angular momentum $m\hbar$ per particle if cylindrically symmetric) by imprinting a

linear azimuthal phase around the ring. Finally, the release of the condensate was simulated by evolving the result of phase (2) using the time-dependent Gross-Pitaevskii equation (TDGPE). Here there were two cases: (3a) direct release, where the TDGPE is evolved with V_{trap} set to zero, or (3b) ramp and release, where the ring-Gaussian potential depth, V_G, is reduced to about 10% of its initial value and then the potential is turned off.

The TIGPE used to obtain the initial condensate, $\psi_0(\mathbf{r})$, has the form

$$-\frac{\hbar^2}{2M}\nabla^2\psi_0 + V_{\text{trap}}(\mathbf{r})\psi_0 + gN|\psi_0|^2\psi_0 = \mu_0\psi_0, \qquad (1)$$

where M is the mass of a (^{23}Na) condensate atom, g is the strength of the atom-atom interaction due to binary scattering, N is the number of condensate atoms, μ_0 is the chemical potential, and V_{trap} is the potential created by external laser beams as described in Sec. II.

The potential is modeled as a superposition of a vertical (z direction) harmonic potential due to the horizontal light sheet and a horizontal (xy plane) ring-Gaussian potential due to the vertical masked-Gaussian laser beam. This potential (in which the energy origin is referenced at the potential minimum) has the form

$$V_{\text{trap}}(\mathbf{r},t) = \tfrac{1}{2}M\omega_z^2 z^2 + f(t)V_G(1 - e^{-2(\rho-\rho_0)^2/w^2}), \qquad (2)$$

where $\rho = \sqrt{x^2 + y^2}$ and $f(t)$ is a function of time that enables simulation of ramp-and-release–type experiments. The parameters in this potential are ω_z, the frequency of the vertical harmonic confinement, and V_G, ρ_0, and w, are, respectively, the depth, radius, and $1/e^2$ width of the ring-Gaussian potential.

For purposes of numerical work, we introduced a set of scaled units and expressed the TIGPE and the TDGPE in terms of scaled variables measured in these units. The scaled units are referenced to a chosen unit of length, denoted by L_0, and scaled spatial coordinates are given by $\bar{x} \equiv x/L_0$, $\bar{y} \equiv y/L_0$, and $\bar{z} \equiv z/L_0$. Energy and time units are defined in terms of L_0, $E_0 \equiv \hbar^2/(2ML_0^2)$, and $T_0 \equiv \hbar/E_0$, enabling the definition of a scaled time: $\bar{t} \equiv t/T_0$. Hereafter barred symbols will denote quantities expressed in their appropriate scaled units.
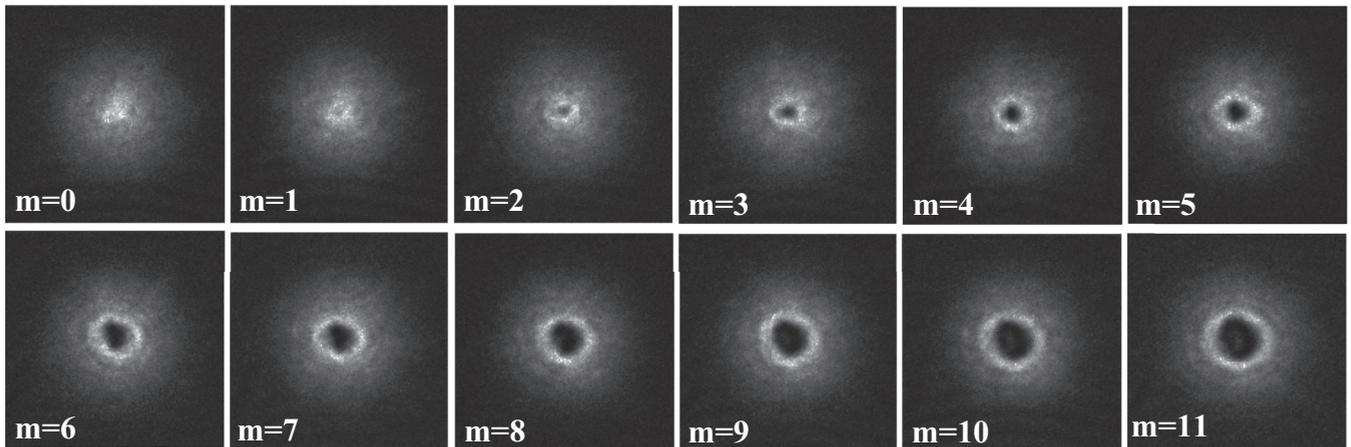

FIG. 3. Time-of-flight images of the condensate after direct release from the trap and 10 ms TOF. Each image is labeled with the circulation m that was determined by analysis of hole size as shown in Fig. 2.
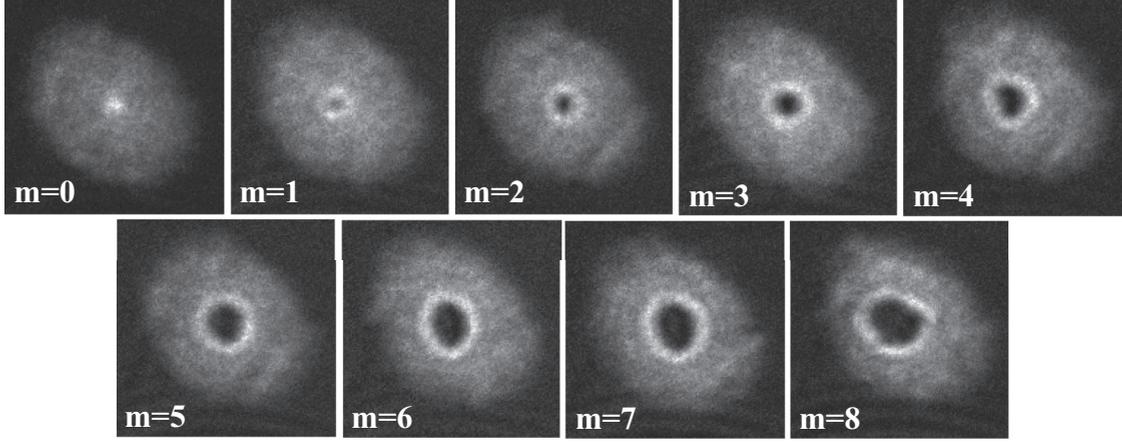
FIG. 4. Time-of-flight images of the condensate after ramp down and release from the trap and 10 ms TOF. Each image is labeled with the circulation m that was determined by analysis of hole size as shown in Fig. 2.

It will also be convenient to express the solution of the TIGPE in terms of scaled units as $\psi_0(\mathbf{r}) \equiv L_0^{-3/2} \bar{\psi}_0(\bar{\mathbf{r}})$. In terms of these variables the TIGPE becomes

$$-\bar{\nabla}^2 \bar{\psi}_0 + \bar{V}_{\text{trap}} \bar{\psi}_0 + \bar{g} N |\bar{\psi}_0|^2 \bar{\psi}_0 = \bar{\mu} \bar{\psi}_0. \tag{3}$$

Here $\bar{g} \equiv g/(E_0 L_0^3)$, $\bar{\nabla}^2 = (\partial^2/\partial\bar{x}^2 + \partial^2/\partial\bar{y}^2 + \partial^2/\partial\bar{z}^2)$ is the Laplacian in terms of scaled variables, and the trap potential takes the form

$$\begin{aligned}\bar{V}_{\text{trap}}(\bar{\mathbf{r}}, \bar{t}) &= \bar{\omega}_z^2 \bar{z}^2 + f(\bar{t}) \bar{V}_G (1 - e^{-2(\bar{\rho} - \bar{\rho}_0)^2/\bar{w}^2}) \\ &\approx \bar{\omega}_z^2 \bar{z}^2 + f(\bar{t}) \bar{\omega}_\rho^2 (\bar{\rho} - \bar{\rho}_0)^2, \end{aligned} \tag{4}$$

where $\bar{\omega}_z \equiv \omega_z/\omega_0$, $\bar{\omega}_\rho = (2\bar{V}_G/\bar{w}^2)^{1/2}$, and ω_0 is the scaled frequency unit that is related to the length unit by $L_0 = (\hbar/M\omega_0)^{1/2}$. The length unit we chose for the results presented here was $L_0 = 10$ μm and, since the condensate was composed of ^{23}Na atoms, the energy unit became $E_0 = 1.444 \times 10^{-33}$ J $= 0.105 k_B$ nK, where k_B is Boltzmann's constant. The time unit was $T_0 = 72.7$ ms and the angular frequency unit was $\omega_0 = 27.5$ rad/s.

To simulate the experiment, the following parameter values were used: $N = 400\,000$ atoms, $\omega_z = 2\pi \times 600$ Hz, $\rho_0 = 18.5$ μm, and $w = 9.45$ μm. These were their experimentally determined values. This left only the potential depth, V_G, undetermined. The value of V_G was obtained by matching the measured density profile of the *in situ* condensate with that predicted by the Gaussian-blurred TIGPE solution. A Gaussian blur was applied to the TIGPE solution by convolving it with a Gaussian having a 4 μm $1/e^2$ width. This measured 2D profile is displayed in Fig. 1(a). After extracting the measured *in situ* density along a cut through the center of the initial-state BEC [see Fig. 1(c)], we solved the TIGPE for various values of V_G and applied a Gaussian blur to each. The value of V_G selected was the one for which the associated Gaussian-blurred TIGPE solution best matched the measured cut-through *in situ* density profile of the initial condensate. The fit produced a value of $V_G/k_B = 31.5$ nK (where k_B is Boltzmann's constant) for the potential depth. The resulting theoretical 2D density profile is shown in Fig. 1(b), and a comparison of experimental, TIGPE, and Gaussian-blurred TIGPE cut-through densities for the final

value of V_G is shown in Fig. 1(c). The values of V_G and w correspond to a radial harmonic frequency of $\omega_\rho \approx 150$ Hz.

The rest of the experiment was simulated by solving the TDGPE, whose form in scaled units is

$$i \frac{\partial \bar{\psi}}{\partial \bar{t}} = -\bar{\nabla}^2 \bar{\psi} + \bar{U}(\bar{\mathbf{r}}, \bar{t}) \bar{\psi} + \bar{g} N |\bar{\psi}|^2 \bar{\psi}. \tag{5}$$

The form of $\bar{U}(\bar{\mathbf{r}}, \bar{t})$ differed depending on whether a direct-release or ramp-and-release experiment was simulated. This will be discussed more fully below. The TDGPE was solved using the split-step Crank-Nicolson algorithm [16] on a 3D xyz spatial grid of $400 \times 400 \times 200$ points which gridded a box of dimensions $20 \times 20 \times 10$ scaled length units. This translated into a box of $200 \times 200 \times 100$ μm, which proved to be large enough to completely eliminate wall-bounce effects. The time of flight (TOF) of condensate expansion was 10 ms in both the direct-release and ramp-and-release cases. The TIGPE solution used to fit the potential parameters was obtained by solving the TDGPE in imaginary time using the same algorithm and grid characteristics.

IV. COMPARISON OF EXPERIMENT WITH GP SIMULATIONS

A. Direct release

The comparison of GP simulations with experiment for the direct-release case is shown in Figs. 5 and 6. Figure 5 depicts the comparison of condensates which were directly released after $1 \leqslant m \leqslant 6$ units of angular momentum have been applied. As noted above, for the simulation curves angular momentum is added to the initial condensate via phase imprint. The initial angular momentum corresponding to the experimental data was determined by analysis of the sizes of the holes in the final image.

Each of the six graphs displays cut throughs of the optical density of the condensate cloud after TOF. In addition to the data (red curves with individual points visible), two simulation curves are plotted. The dashed (green) line is a cut through of the density predicted by the TDGPE. The solid (blue) line is a cut through of the TDGPE prediction convolved with a Gaussian with a 4 μm $1/e^2$ radius. Applying this average to
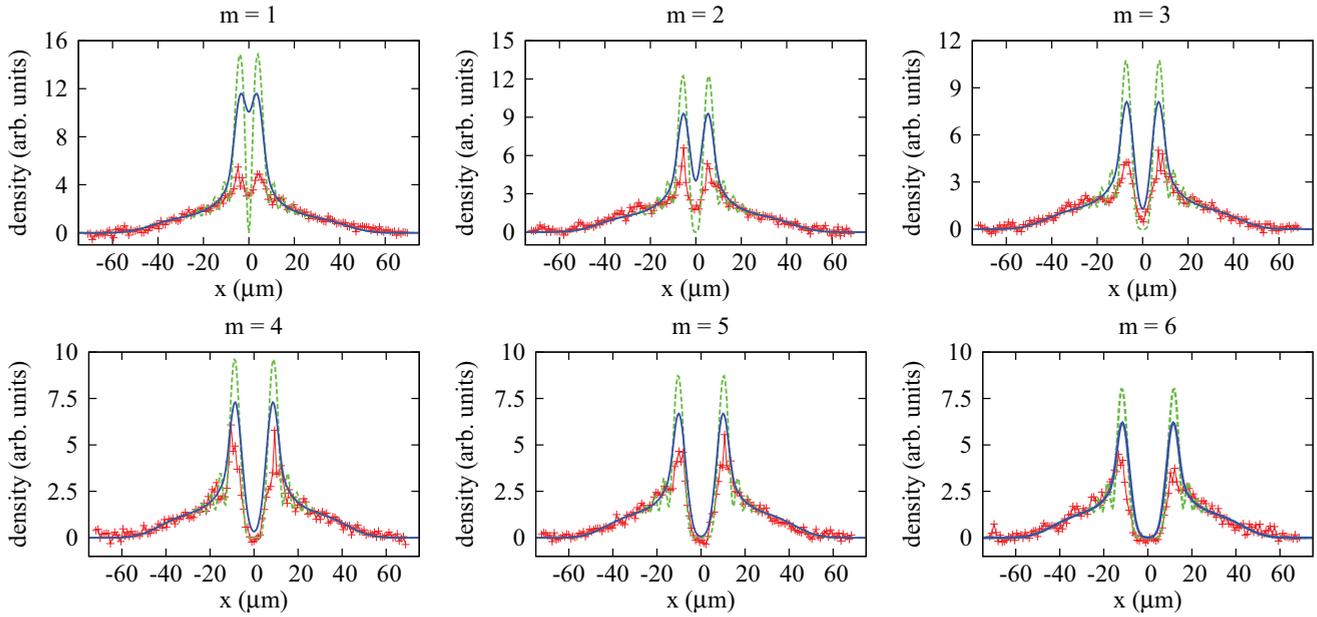
FIG. 5. (Color online) Comparison of the cut through of the condensate optical density data (shown as individual points connected with a solid red line) after direct release and 10 ms TOF with GP simulations for initial circulations $m = 1, \ldots, 6$. Two theoretical curves appear in each graph. The dotted (green) curve is the result of evolving the 3D TDGPE. The solid (blue) curve is a cut through of the TDGPE prediction convolved with a Gaussian having a 4 μm $1/e^2$ radius to account for the finite resolution of the experimental instrument.

the theoretical results accounts for the finite resolution of the imaging optics in the NIST experiment. Figure 6 displays the identical comparison for the cases $7 \leqslant m \leqslant 12$.

To create the comparisons shown in Figs. 5 and 6 both the experimental data and the theoretical results were subjected to some postprocessing. Extracting the experimental cut through from the raw images involved comparing cut-through data along different lines through each image. The most symmetric and highest amplitude density data was selected as the best

representative data for each image. This amounted to an estimate of the location within each image of the center of the trap. When creating the comparison plots of experiment with GP simulations, we shifted the experimental data left-right so that the center of the trap in the data coincided with the theoretical origin of coordinates.

We also processed the simulation results by multiplying them by an overall normalization constant. This was necessary because the raw experimental data was expressed in arbitrary
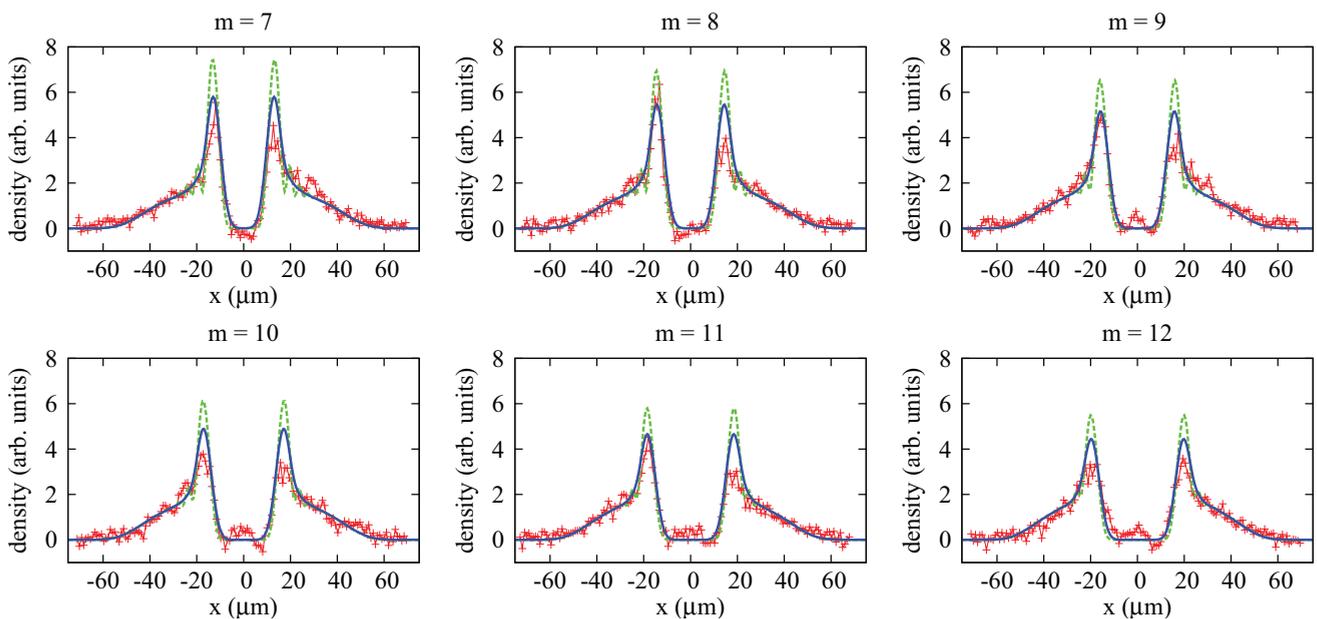

FIG. 6. (Color online) Comparison of the cut through of the condensate optical density data after direct release and 10 ms TOF with GP simulations for initial circulations $m = 7, \ldots, 12$.

units and the normalization of the simulation results amounted to a units conversion. We determined a normalization constant, N_{dr}, for the direct-release case by fitting the tail of the $m = 1$ density profile. This normalization constant was then applied to the theoretically determined density profiles for all other m values in the direct-release case without further adjustment. The same procedure of fitting the tail of the $m = 1$ density profile was followed in the ramp-and-release case to obtain a normalization constant, N_{rr}, and this value was applied to the density profiles of all other m values. The values of N_{dr} and N_{rr} were not the same.

As seen in Figs. 5 and 6, direct release and subsequent expansion of a stirred ring BEC results in an annulus-shaped optical density image when viewed from above. One can see that the agreement between the GP simulation results and experiment is very good for directly released condensates. This is especially the case when the instrument resolution is accounted for. For all m values, the size of the hole increases with initial angular momentum and the agreement of experimental hole size with the GP simulations is especially good. We also find good agreement out in the wings of the distribution. Peak-height agreement is not as good; however, this may be due to variations in potential-well depth around the ring.

B. Ramp and release

To model the ramp down, the potential depth of the initial trap was ramped down to 10% of its initial value over 50 ms. The condensate was then released and allowed to expand for 10 ms TOF. The experiment-simulation comparison for this case is shown in Fig. 7. This figure contains six comparison graphs in the same format as in Figs. 5 and 6 where the initial angular momentum ranges over $1 \leqslant m \leqslant 6$. The experimental data and the results of the GP simulation were processed in the same way as for the direct release cases.

For the ramp-down case we find that there is less good agreement in the tails of the distribution than in the direct-release case but that peak sizes and especially hole sizes match quite well. It is also clear that the sizes of the holes are larger for the same m value than in the direct-release case. Thus ramping down the strength of the radial confinement provides a better experimental signature of the initial circulation than direct release.

The agreement between the experimental data and the predictions of the TDGPE indicates that mean-field theory is adequate to understand how hole sizes in the expanded cloud can be used as signatures of condensate circulation before release. Thus it follows that we should be able to rely on the TDGPE to also be a reliable predictor of the dynamics of the condensate cloud after release. This conclusion may be contrasted with recent work [17–20], which indicates that some of the dynamics of the *in situ* cloud (e.g., phase slippage due to vortex dynamics) may not be as well predicted by zero-temperature mean-field theory.

V. BEHAVIOR OF THE RELEASED RING BEC

A. Expansion dynamics

The dynamical behavior of a released ring condensate is illustrated in Figs. 8(a)–8(f). These figures consist of a sequence of cut throughs of the optical density as a function of time after release. Four units of angular momentum ($m = 4$) have been added to the initial BEC. At the moment of release the condensate has the shape of the initial ring [Fig. 8(a)]. After release the condensate expands rapidly inward and more slowly outward. The inward expansion proceeds until the hole reaches a minimum radius [Fig. 8(b)]. When the hole reaches its minimum size (which depends upon the initial angular momentum of the condensate), the density around the edge of the hole begins to increase rapidly as seen in Fig. 8(c). As
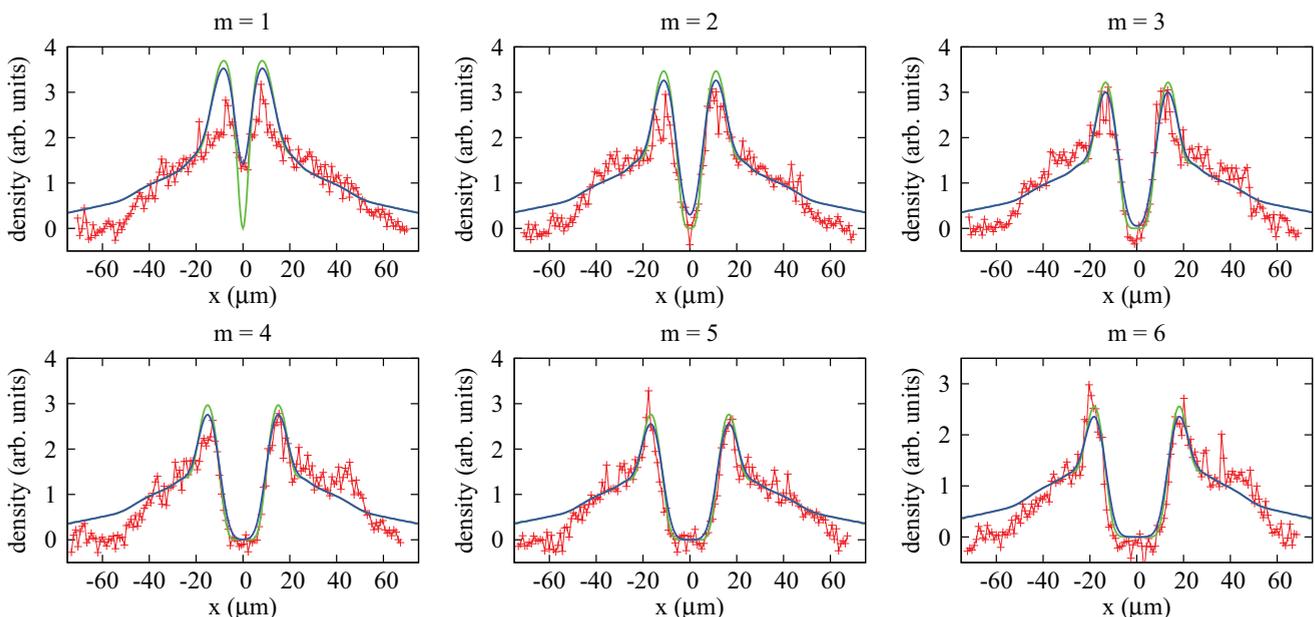

FIG. 7. (Color online) Comparison of the cut through of the condensate optical density data after ramp down and release and 10 ms TOF with GP simulations for initial circulations $m = 1, \ldots, 6$.
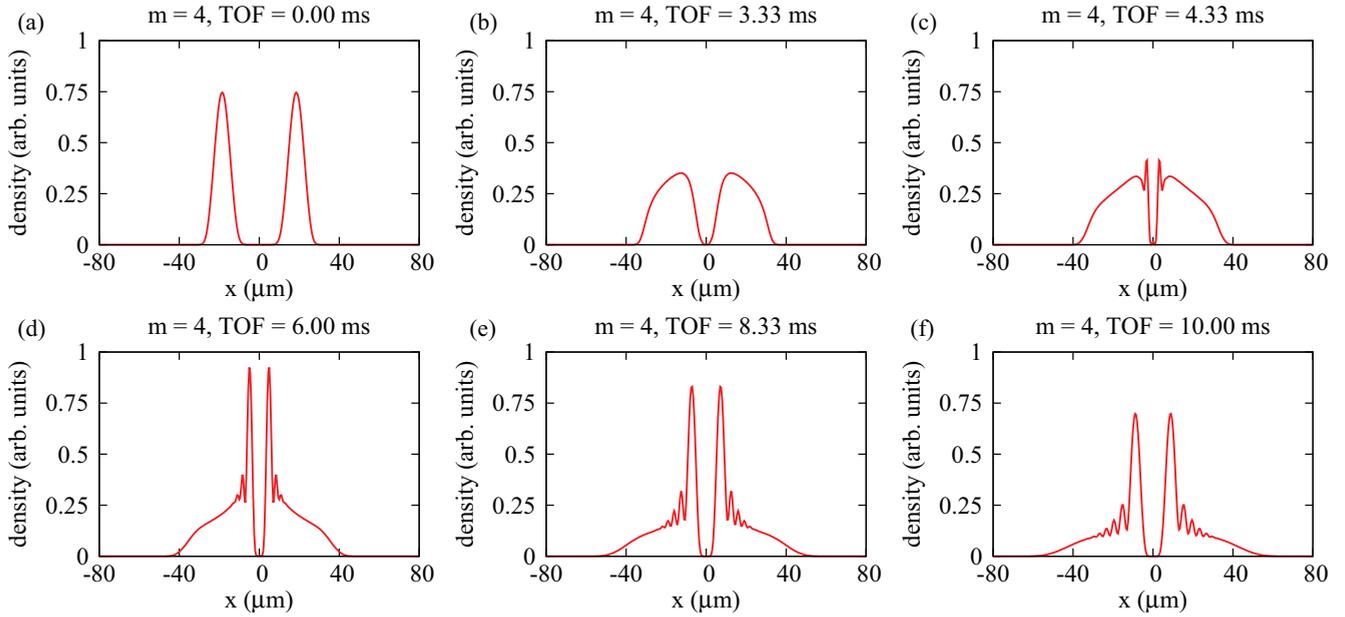
FIG. 8. (Color online) Sequence of cut throughs of the optical density as a function of time after direct release depicting the dynamics of the expansion. The initial condensate was phase imprinted with four units of angular momentum.

the density around the edge grows toward its maximum height, a series of density rings begins to form [Fig. 8(d)]. As the peak density begins slowly to decrease, the size of the central hole begins increasing and more rings form as seen in Figs. 8(e) and 8(f). In the limit of large times (not shown), the peak flattens out and the condensate shape takes the form of a large central hole surrounded by a density plateau which is, in turn, surrounded by a series of density rings.

The appearance of rings during the rapid increase of the density around the edge of the hole seems to be an interference effect. Condensate atoms flow in towards the edge of the hole and then flow out as evidenced by the rapid increase and subsequent slower decrease of the density maximum. At a fixed distance (but larger than the hole radius) from the center of the condensate, condensate atoms can arrive there by two distinct pathways. Either they are flowing in towards the edge of the hole or they are flowing back out having already visited the hole edge. These two possibilities create two pathways to the same location and thus exhibit quantum interference.

This dynamical behavior also highlights an essential difference between simply and multiply connected condensates. In simply connected condensates the velocity distribution can generally be probed by release and subsequent imaging of the density profile. This works as long as interactions between condensate atoms during the expansion can be neglected. It is clear that this is not the case for ring condensates.

B. Hole size scaling with winding number

It is interesting to compare the theoretical predictions for the scalings of the hole sizes with initial winding numbers for the direct-release case with the ramp-and-release case. Figure 9 displays the scalings for the two cases. The lower curve in that figure shows the radii, $R_{\text{direct}}(m)$, of the holes versus winding number for the direct-release case for $m = 0, \ldots, 12$. The hole radius was defined to be 40% of the peak density and this

percentage was chosen so that the extrapolation of the radii back to $m = 0$ went through zero. The solid line that also appears in the lower curve of Fig. 9 is a linear fit [$R_{\text{direct}}(m) = am + b$] to the hole radii. The values of the fit parameters were $a = 1.342\,68$ μm and $b = 0.073\,2567$ μm. Thus hole radii for the direct-release case appear to scale linearly with the initial circulation of the ring BEC over the entire range of m.

The ramp-and-release case shows a different scaling and the radii versus m, $R_{\text{ramp}}(m)$, are shown in the upper curve of Fig. 9. Here the same definition of hole radius was used. However, the
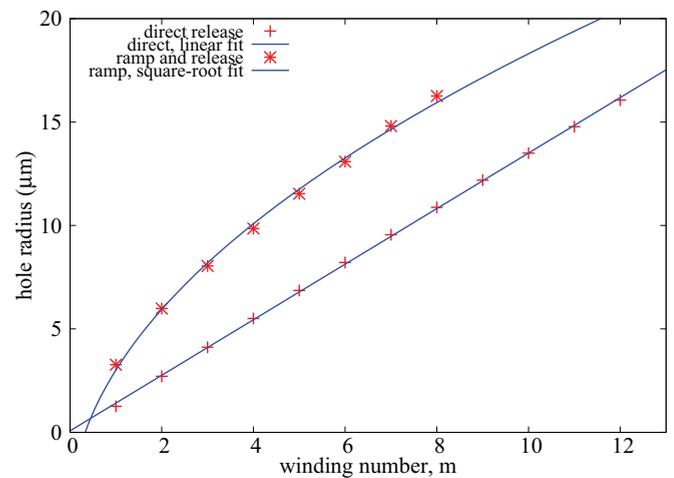

FIG. 9. (Color online) Hole size scaling as a function of initial winding number as predicted by the TDGPE. The hole radius was defined by the point at which the optical density reached 40% of its peak value closest to the trap axis. The lower curve displays hole radii for the direct-release simulations (plus symbols). The solid line appearing in the lower curve is a fit to the direct-release radii to the function $am + b$. The upper curve shows corresponding results for the ramp-and-release case. The asterisks depict the radii, while the solid curve is a fit of the ramp-and-release hole radii to the function $\alpha\sqrt{m} + \beta$.

radii do not appear to be linear. This conclusion is supported by the accompanying solid line which is a fit to a linear function of the square root of m: $R_{ramp}(m) = \alpha\sqrt{m} + \beta$. The result of the fit yielded $\alpha = 7.069\,04$ μm and $\beta = -4.052\,76$ μm.

We hasten to emphasize that the scalings (i.e., linear or square root) of the hole radii with winding number were independent of our definition of the hole radius. We defined the hole radius as the location where the condensate density reached 40% of the peak density. We chose that so that the particular straight line observed in the direct release case went through zero radius for $m = 0$ when extrapolated. Choosing a different percentage of the peak density for the hole radius criterion also exhibited linear scalings with different y intercepts. While we adhered to this definition of hole radius for the ramp-and-release case, we also found that the square-root scaling did not depend on the hole radius definition.

One effect of these different scalings is that the hole *areas* for the direct-release case will scale approximately quadratically with m while the hole areas for the ramp-and-release case will scale approximately linearly with m. The exact scaling, however, depends on the particular definition of the hole radius. Evidence of this effect can be seen in Fig. 2 where histograms of the experimental hole areas are shown. In Fig. 2(a), which shows the direct-release hole areas, the intervals between hole-area clusters can be seen to grow larger as m increases. In the ramp-and-release case, shown in Fig. 2(b), these intervals seem to stay the same as m increases. This supports the conclusion that direct-release hole areas scale approximately quadratically with m, while ramp-and-release areas scale approximately linearly with m.

VI. CONCLUSION

In this paper we have shown by comparing experiment with the results of simulations based on the GP equation how the circulation of a stirred ring Bose-Einstein condensate can be probed by measuring the size of the hole after release and expansion. We found that the experimental data and the predictions of the time-dependent Gross-Pitaevskii equation for the sizes of holes produced by stirred and released condensates agree well over a large range of winding numbers. This was the case for condensates released directly after stirring and also after ramp down.

We also used the agreement with the TDGPE to understand the dynamics of the condensate after release. We found that the hole of the ring is initially filled in to a minimum radius that depends on the winding number at release time. Density around the edge of the minimum-radius hole increases to a maximum and then begins to decrease. Just after the time of maximum density interference rings begin to appear. Since atoms flow in and then flow out, the rings seem to be due to interference between atoms that are flowing in and those flowing out.

Ring condensates have exhibited phenomena such as persistent currents and deterministic phase slips which came as the result of stirring [13,14]. In the latter case, the system was modeled as an "atom circuit" in which the phase changes that occur when traversing a closed path around the ring sum to a definite and known quantized value. The key to evaluating these models is the ability to determine the winding experimentally and correlating observed condensate behavior with that predicted by the model. Such models will be essential in understanding the behavior of future "atomtronic" systems based on Bose-Einstein condensates confined in ring potentials.

[1] R. A. Pepino, J. Cooper, D. Z. Anderson, and M. J. Holland, Phys. Rev. Lett. **103**, 140405 (2009).

[2] B. T. Seaman, M. Krämer, D. Z. Anderson, and M. J. Holland, Phys. Rev. A **75**, 023615 (2007).

[3] A. Ruschhaupt and J. G. Muga, Phys. Rev. A **70**, 061604 (2004).

[4] J. J. Thorn, E. A. Schoene, T. Li, and D. A. Steck, Phys. Rev. Lett. **100**, 240407 (2008).

[5] J. A. Stickney, D. Z. Anderson, and A. A. Zozulya, Phys. Rev. A **75**, 013608 (2007).

[6] J. G. Lee, B. J. McIlvain, C. J. Lobb, and W. T. Hill, III, Sci. Rep. **3**, 1034 (2013).

[7] J.-P. Brantut, J. Meineke, D. Stadler, S. Krinner, and T. Esslinger, Science **337**, 1069 (2012).

[8] J. Clarke and A. I. Braginski, *The SQUID Handbook*, Vols. 1 and 2 (Wiley-VCH, Weinheim, 2004).

[9] K. K. Likharev, Rev. Mod. Phys. **51**, 101 (1979).

[10] J. C. Davis and R. E. Packard, Rev. Mod. Phys. **74**, 741 (2002).

[11] M. Albiez, R. Gati, J. Fölling, S. Hunsmann, M. Cristiani, and M. K. Oberthaler, Phys. Rev. Lett. **95**, 010402 (2005).

[12] S. Levy, E. Lahoud, I. Shomroni, and J. Steinhauer, Nature (London) **449**, 579 (2007).

[13] A. Ramanathan, K. C. Wright, S. R. Muniz, M. Zelan, W. T. Hill, C. J. Lobb, K. Helmerson, W. D. Phillips, and G. K. Campbell, Phys. Rev. Lett. **106**, 130401 (2011).

[14] K. C. Wright, R. B. Blakestad, C. J. Lobb, W. D. Phillips, and G. K. Campbell, Phys. Rev. Lett. **110**, 025302 (2013).

[15] The decay time for vortex excitations in the annulus varies with experimental conditions, but is typically ≈ 3 s.

[16] P. Muruganandam and S. K. Adhikari, Comput. Phys. Commun. **180**, 1888 (2009).

[17] F. Piazza, L. A. Collins, and A. Smerzi, Phys. Rev. A **80**, 021601 (2009).

[18] A. C. Mathey, C. W. Clark, and L. Mathey, arXiv:1207.0501.

[19] F. Piazza, L. A. Collins, and A. Smerzi, J. Phys. B **46**, 095302 (2013).

[20] S. Eckel, J. G. Lee, F. Jendrzejewski, N. Murray, C. J. Lobb, M. Edwards, W. D. Phillips, and G. K. Campbell (unpublished).